

Simulation of Deformation and Fracture in Polycrystalline Aluminum Alloy under Dynamic Loading

R. R. Balokhonov^{1*}, M. V. Sergeev¹, and V. A. Romanova¹

¹ *Institute of Strength Physics and Materials Science, Siberian Branch, Russian Academy of Sciences, Tomsk, 634055 Russia*

* *e-mail: rusy@ispms.ru*

Received October 5, 2022; revised November 24, 2022; accepted November 24, 2022

Abstract—A numerical study is conducted on the influence of the polycrystalline structure, strain rate, and constrained boundary conditions on the plastic strain localization and fracture of 6061-T6 aluminum alloy under dynamic loading. The investigation is carried out on a three-dimensional polycrystalline structure generated by the step-by-step packing method. The deformation behavior of 6061-T6 aluminum alloy under different strain rates and temperatures is described using a relaxation constitutive equation. The initiation and growth of cracks are taken into account using a strain criterion. The developed models and polycrystalline structure are implemented into the ABAQUS/Explicit finite element package to simulate tension of the aluminum samples. It is shown that taking into account the polycrystalline structure leads to lower values of the macroscopic yield stress in comparison with a homogeneous sample. The strain rate and constrained boundary conditions are shown to affect the crack initiation site and fracture patterns.

Keywords: dynamic loading, polycrystals, aluminum alloys, numerical simulation, plastic strain, fracture

DOI: 10.1134/S1029959923030037

1. INTRODUCTION

Aluminum alloys are widely used in the aerospace, aviation, and automotive industries due to high specific strength [1, 2] and ability to operate under thermomechanical loads in a wide range of strain rates. The most commonly used alloys are of 6061 series, in particular, Al6061-T6 [1, 3].

The dynamic deformation of alloys is described using relaxation constitutive relations, which can generally be divided into two main categories [4, 5]: macrophenomenological and physically based ones. Macrophenomenological models are simple and include a relatively small number of parameters that have no physical meaning and are determined by simple approximation of experimental data. However, their application is limited by the lack of physical validity. For example, there are certain ranges of strain rates and temperatures for most of these models within which the results obtained with the model are consistent with experimental data. Therefore, each model is usually suitable for describing a particular alloy or a limited group of alloys [6]. The literature contains many macrophenomenological constitutive models, such as Johnson–Cook [7], Khan–

Huang [8], Khan–Huang–Liang [9], Bodner–Partom [10], Fields–Bachofen [11], and their modifications proposed for more accurate predictions [6, 12, 13].

Physically based models are used to account for the microstructural evolution of the material, dislocation dynamics, and thermal activation at high strain rates and temperatures. They can more accurately determine the material behavior in a wide range of loading conditions, but deal with a relatively large number of material constants. There are many physically based models, such as Zerilli–Armstrong [14], dynamic recrystallization [15], Preston–Tonks–Wallace [16], Rusinek–Klepaczko [17], and Voyiadjis–Almasri [18]. The thermomechanical model of Nemat-Nasser and Guo [19] is based on the dislocation theory of plastic flow in metals, takes into account the effect of temperature and strain rate, and was successfully applied to describe the dynamic deformation of steels [20]. In the present paper, this model is used to study the dynamic deformation and fracture of 6061-T6 aluminum alloy. Fracture of metallic materials is modeled within the framework of various theories, including continuum damage mechanics, Gurson–Tvergaard–Needleman, and other phenome-

nological models [21–24]. In [23], the damage accumulation function depends on temperature, strain rate, and the size of dynamically recrystallized grains. In this work, a strain fracture criterion is used, taking into account the type of stress state.

Real materials have polycrystalline structure, which affects their deformation and fracture behavior because grain boundaries and triple grain junctions are additional sources of stress concentration. Thus, for a reliable prediction of material deformation, in addition to the strain rate and temperature, it is necessary to account for the structural heterogeneity of the material.

There are well-known methods for modeling heterogeneous structures, such as Monte Carlo [25], front tracking [26], Voronoi–Delaunay [27], cellular automata [28], etc. Some of these methods have been successfully used in recent decades for modeling three-dimensional structures. However, increasing spatial dimensions, memory and computation time requirements call for the modification and optimization of the basic algorithms of existing methods and development of new methods. Here we generated three-dimensional polycrystals using our previously developed step-by-step packing method [29]. The basic idea of the method is that the material volume is incrementally filled with structural elements in accordance with a given nucleus growth law. The growth laws are chosen so that the morphology of the model structure conforms to the experimentally observed one. It is shown that in the case of a polycrystalline structure the spherical growth law can be applied to obtain the grain shape and grain size distributions close to the experimental ones.

There exist various models for studying the stress-strain state of materials with explicit consideration of the polycrystalline structure. The parameters of each grain can be set based on its actual physical properties, such as lattice orientation and mechanical characteristics. This approach is used in crystal plasticity theory. Crystal plasticity models are often used to predict the effective properties of bulk polycrystals, e.g., in [30], where two types of three-dimensional polycrystalline microstructures are considered: (i) idealized structures with cubic grains, and (ii) realistic polycrystals built on the basis of a kinetic Monte Carlo model.

Thus, for a reliable description of dynamic deformation behavior by numerical simulations, it is necessary to take into account the structure, plastic strain localization, possible crack initiation and growth, the velocity and temperature sensitivity of

the material, and the influence of boundary conditions. The simultaneous effect of all these factors has not been reported so far in the literature. The deformation of various materials was studied by finite element and molecular dynamics simulations taking into account the polycrystalline structure and temperature [31–33] or strain rate [34–36]. In [37], EBSD data were used for finite element modeling of the anisotropic mechanical properties of polycrystalline tantalum. The methodology of the present work is closest to that of paper [38], where the deformation of a polycrystalline structure is modeled and the relaxation model parameters are selected based on tensile tests of 6061 and 5052 aluminum alloys at different strain rates and temperatures without considering fracture. Then crystal plasticity and damage evolution models are used to describe macroscopic necking behavior of a tensile specimen, without considering its polycrystalline structure but with specifying a random uniform law of lattice orientation distribution approximated by finite elements.

Previously we studied the plastic strain localization and fracture of polycrystalline metals and alloys, as well as composites with polycrystalline or homogeneous matrices under quasi-static loading conditions [29, 39–42]. Here we investigate the plastic deformation behavior and crack initiation and growth in Al6061-T6 alloy polycrystals depending on the strain rate and constrained deformation conditions.

2. PHYSICAL AND MATHEMATICAL FORMULATION OF THE PROBLEM

A three-dimensional dynamic problem was solved to study the influence of the structure, strain rate, and additional boundary conditions on the stress/strain distribution and fracture behavior of an aluminum alloy. The general system of equations includes the momentum conservation law, the continuity equation, and strain rate relations. The structure of a polycrystalline sample was generated by the step-by-step packing method. The dynamic response of aluminum was described using a relaxation constitutive equation based on the concept of dislocation mediated plastic flow. The fracture of local regions of the polycrystal was taken into account using the criterion of maximum equivalent plastic strain. The structure and model were implemented into ABAQUS/Explicit. The deformation and fracture of the polycrystalline structure were simulated to investigate the influence of strain rate and loading conditions on strain localization and cracking.

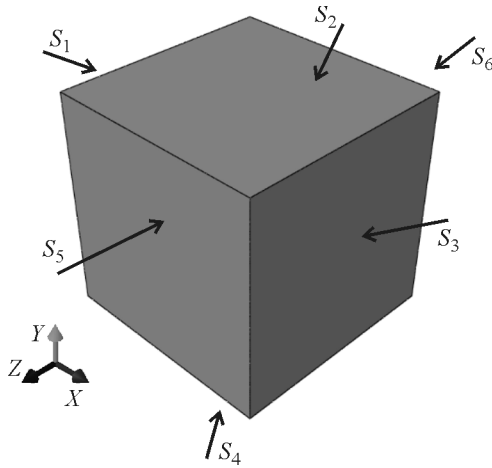


Fig. 1. Schematic of sample stretching.

2.1. Thermomechanical Relaxation Constitutive Equation

The system of equations is closed by Hooke's law constitutive equations that define the relationship between the stress and strain rates:

$$\begin{aligned} \dot{\sigma}_{ij} &= -\dot{P}\delta_{ij} + \dot{S}_{ij} \\ &= K\dot{\varepsilon}_{kk}\delta_{ij} + 2\mu(\dot{\varepsilon}_{ij} - \dot{\varepsilon}_{kk}\delta_{ij}/3 - \dot{\varepsilon}_{ij}^p), \end{aligned} \quad (1)$$

where $\dot{\varepsilon}_{ij} = 1/2(v_{i,j} + v_{j,i})$, v_i are the mass velocity vector components, σ_{ij} , S_{ij} , ε_{ij} , and ε_{ij}^p are the components of the Cauchy stress tensor, deviatoric stress tensor, total logarithmic strain tensor, and logarithmic plastic strain tensor in the Cartesian coordinate system of the sample (Fig. 1), P is the pressure, K and μ are the elastic bulk and shear moduli, and δ_{ij} is the Kronecker delta. The upper dot denotes the material derivative, and the repeated index convention for summation is used.

The plastic strain rate $\dot{\varepsilon}_{ij}^p$ is determined by considering the effective stress as the sum of the athermal and thermal components [19]:

$$\begin{aligned} \sigma_{\text{eq}} &= \sigma_{\text{eq}}^a + \sigma_{\text{eq}}^T \\ &= \sigma_s - (\sigma_s - \sigma_0) \exp(\varepsilon_{\text{eq}}^p / \varepsilon_r^p) + \sigma_{\text{cold}} \\ &\times \left[1 - \left(\frac{k \left(T_0 + \int_0^{\varepsilon_{\text{eq}}^p} \frac{\beta}{\rho C_v} \sigma_{\text{eq}} d\varepsilon_{\text{eq}}^p \right)}{G_0} \ln \frac{\dot{\varepsilon}_{\text{eq}}^p}{\dot{\varepsilon}_r^p} \right)^{1/q} \right]^{1/d}, \end{aligned} \quad (2)$$

where σ_{eq} and $\varepsilon_{\text{eq}}^p$ are the equivalent stress and the accumulated equivalent plastic strain:

$$\sigma_{\text{eq}} = 1/\sqrt{2} [(\sigma_{xx} - \sigma_{yy})^2 + (\sigma_{yy} - \sigma_{zz})^2$$

Initial conditions

$$\rho|_N = \rho_0, \varepsilon_{ij} = 0, \sigma_{ij} = 0, t = 0.$$

Boundary conditions (simple uniaxial tension)

$$\begin{aligned} \dot{u}_x(x, y, z, t) &= \text{const} = v, \quad t \geq 0, (x, y, z) \in S_3, \\ \dot{u}_x(x, y, z, t) &= \text{const} = -v, \quad t \geq 0, (x, y, z) \in S_1, \\ \sigma_{ij}(x, y, z, t) \cdot n_j &= 0, \quad t \geq 0, (x, y, z) \in S_2 \cup S_4 \cup S_5 \cup S_6, \\ \sigma_{xy}(x, y, z, t) &= 0, \quad t \geq 0, (x, y, z) \in S_1 \cup S_3, \\ \sigma_{xz}(x, y, z, t) &= 0, \quad t \geq 0, (x, y, z) \in S_1 \cup S_3. \end{aligned}$$

Quasi-plane strain conditions

$$\begin{aligned} \dot{u}_z(x, y, z, t) &= 0, \quad t \geq 0, (x, y, z) \in S_5 \cup S_6, \\ \sigma_{zx}(x, y, z, t) &= 0, \quad t \geq 0, (x, y, z) \in S_5 \cup S_6, \\ \sigma_{zy}(x, y, z, t) &= 0, \quad t \geq 0, (x, y, z) \in S_5 \cup S_6. \end{aligned}$$

$$+ (\sigma_{zz} - \sigma_{xx})^2 + 6(\sigma_{xy}^2 + \sigma_{yz}^2 + \sigma_{zx}^2)]^{1/2}, \quad (3)$$

$$\begin{aligned} \varepsilon_{\text{eq}}^p &= \frac{\sqrt{2}}{3} \int_0^t \{ (\varepsilon_{xx}^p - \varepsilon_{yy}^p)^2 + (\varepsilon_{yy}^p - \varepsilon_{zz}^p)^2 \\ &+ (\varepsilon_{zz}^p - \varepsilon_{xx}^p)^2 + 6[(\varepsilon_{xy}^p)^2 + (\varepsilon_{yz}^p)^2 + (\varepsilon_{zx}^p)^2] \}^{1/2} dt; \end{aligned} \quad (4)$$

σ_{eq}^a does not depend on the strain rate and temperature, is due to long-range effects, and can be related to the dislocation density, grain size, formation of substructures, etc. Here we apply a phenomenological isotropic hardening function, where σ_s and σ_0 have the meaning of ultimate strength and yield strength, ε_r^p defines the current value of the strain hardening coefficient, and σ_{eq}^T is associated with short-range barriers to dislocation motion. Using an associated plastic flow rule in the form

$$\dot{\varepsilon}_{ij}^p = \frac{3}{2} \frac{\dot{\varepsilon}_{\text{eq}}^p}{\sigma_{\text{eq}}} S_{ij}$$

and expressing $\dot{\varepsilon}_{\text{eq}}^p$ from Eq. (2), we obtain

$$\dot{\varepsilon}_{ij}^p = \frac{3}{2} \frac{S_{ij}}{\sigma_{\text{eq}}} \dot{\varepsilon}_r^p \exp \left(-\frac{G_0}{kT} \left[1 - \left(\frac{\sigma_{\text{eq}} - \sigma_{\text{eq}}^a}{\sigma_{\text{cold}}} \right)^d \right]^q \right), \quad (5)$$

where σ_{cold} is the stress at which dislocations overcome the barrier without thermal activation, G_0 is the energy sufficient for barrier overcoming only due to thermal activation, and T is the current temperature:

$$T = T_0 + \int_0^{\varepsilon_{\text{eq}}^p} \frac{\beta}{\rho C_v} \sigma_{\text{eq}} d\varepsilon_{\text{eq}}^p,$$

T_0 is the initial temperature (temperature of the medium in dynamic loading tests of samples), $\beta \cong 1$ by many estimates, ρ is the density, $C_v = 0.92 \text{ J/(g K)}$ is

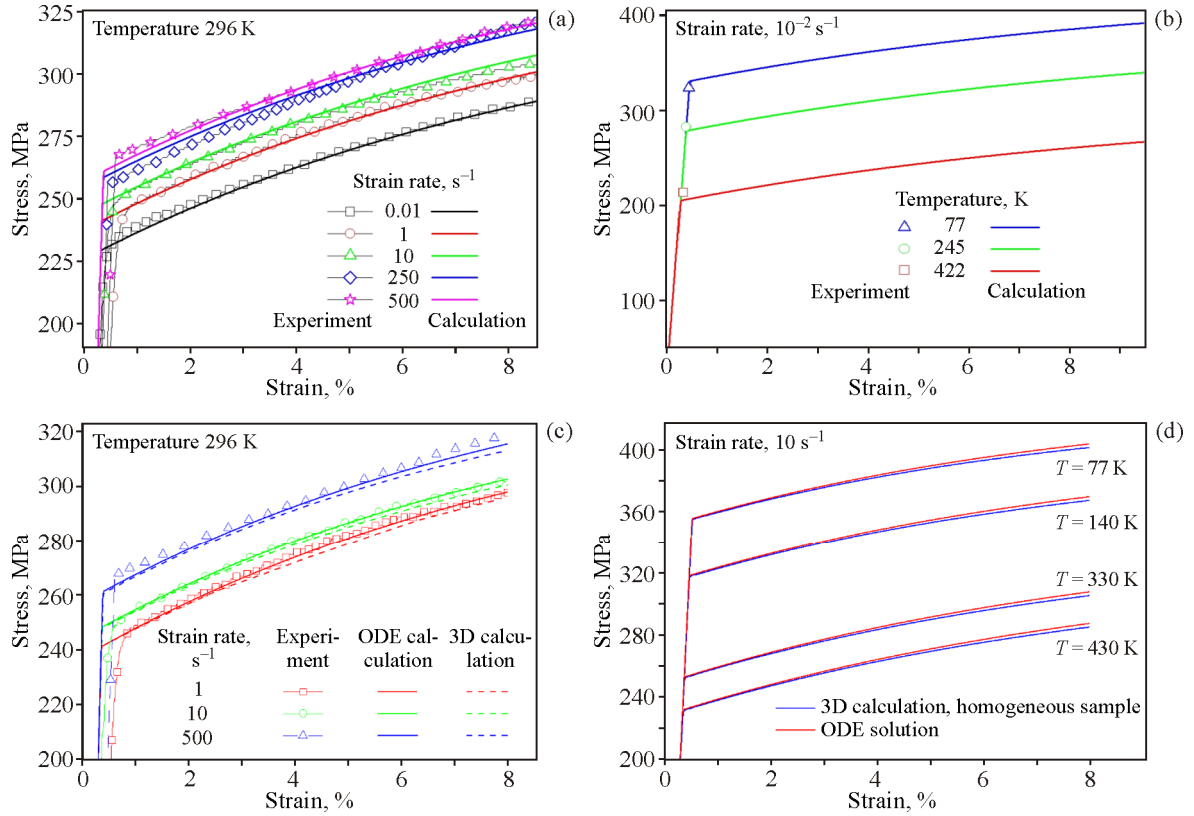


Fig. 2. Experimental and numerical flow curves of Al6061-T6 aluminum alloy at different strain rates (a, c) and predicted flow curves at different test temperatures (b, d) (color online).

the heat capacity, $q=2$ and $d=2/3$ for many metals [19], and k is the Boltzmann constant.

Fracture of aluminum occurs when the equivalent plastic strain reaches the critical value ψ :

$$\varepsilon_{\text{eq}}^{\text{p}} = \psi. \quad (6)$$

If condition (6) is satisfied, $\sigma_{ij}=0$ in the local regions of bulk tension, while in the regions of bulk compression the material cannot resist only shear: $S_{ij}=0$. The constant ψ can be determined experimentally by measuring sample deformation at the prefracture stage. The implementation of Eqs. (1), (5), and (6) into the boundary value calculations in ABAQUS/Explicit was carried out through the VUMAT subroutine.

2.2. Initial and Boundary Conditions

Calculations were performed for two types of boundary conditions simulating uniaxial tension of samples with free and constrained side surfaces (constrained boundary conditions). In both calculations, uniaxial tension along the X axis was modeled by setting constant velocities on two opposite surfaces of

the sample. The side surfaces were free from external load or were considered as symmetry planes in the constrained samples (Fig. 1).

2.3. Thermomechanical Model Parameters

The constants in constitutive equation (5) are determined from uniaxial tensile tests. Under uniaxial loading, one stress tensor component is nonzero in the X direction, and the strain tensor components in the Y and Z directions coincide and are proportional to the component in the X direction:

$$\begin{aligned} \dot{\sigma}_x \neq 0 &= \dot{\sigma}_{\text{eq}} = \dot{\sigma}, \\ \dot{\varepsilon}_y &= \dot{\varepsilon}_z = -\nu \dot{\varepsilon}_x = -\nu \dot{\varepsilon}, \\ \dot{\varepsilon}_y^{\text{p}} &= \dot{\varepsilon}_z^{\text{p}}, \quad \dot{\varepsilon}_x^{\text{p}} = \dot{\varepsilon}^{\text{p}}, \end{aligned} \quad (7)$$

where ν is the Poisson ratio. Taking into account the assumption of plastic incompressibility

$$\dot{\varepsilon}_{kk}^{\text{p}} = 0, \quad (8)$$

Eq. (1) can be written as

$$\dot{\sigma} = E(\dot{\varepsilon} - \dot{\varepsilon}^{\text{p}}), \quad (9)$$

where Eq. (5), taking into account Eq. (7), reads

Table 1. Model parameters in Eqs. (5), (6), and (10)

ρ_0 , g/cm ³	σ_s , MPa	σ_0 , MPa	ε_r^p , %	K , GPa	μ , GPa	$\dot{\varepsilon}_r^p \times 10^{12}$, s ⁻¹	k/G_0 , K ⁻¹	σ_{cold} , MPa	ψ , %
2.7	332	234	9.5	66	26	2.5	6.1×10^{-5}	280	10

$$\dot{\varepsilon}^p = \dot{\varepsilon}_r^p \exp \left(-\frac{G_0}{kT} \left[1 - \left(\frac{\sigma - \sigma^a}{\sigma_{\text{cold}}} \right)^d \right]^q \right), \quad (10)$$

where

$$\sigma^a = \sigma_s - (\sigma_s - \sigma_0) \exp(\varepsilon_r^p / \varepsilon_r^p).$$

Ordinary differential equations (ODE) (9) and (10) were solved numerically by the fourth-order Runge–Kutta method. The parameter values were chosen by solving a series of direct problems in such a way that the calculated σ – ε curves coincided with the experimentally observed mechanical behavior of Al6061-T6 aluminum alloy at different strain rates and temperatures (Figs. 2a and 2b). The computation time can be reduced by orders of magnitude if the optimal values of the model parameters are determined by solving Eq. (10) instead of solving boundary value problems. Initially, the values of σ_s , σ_0 , and ε_r^p were calculated by approximating the experimental quasi-static flow curve. Then, $\dot{\varepsilon}_r^p$, σ_{cold} , and G_0 were varied so that the numerical values coincided with the experimental ones in the specified range of strain rates and temperatures. The found optimal value of G_0 was of the order of the activation energy of vacancy formation in aluminum. The critical strain ψ corresponded to the beginning of the descending portion of the experimental flow curves. Dynamic tensile tests on aluminum specimens were carried out at the University of Stuttgart, Germany. The model parameters are given in Table 1. The determined model constants were used for three-dimensional direct numerical simulations modeling the stretching of homogeneous samples. The simulation results are in good agreement with the ODE calculations and experiment (Figs. 2c and 2d).

Aluminum is a quasi-isotropic material with the elastic anisotropy factor of about 20%. Dislocations can move along several planes during plastic deformation, which promotes multiple slip and, accordingly, quasi-isotropic flow and strain hardening. Therefore, the elastic moduli, ultimate strength, and yield strength for individual grains of the polycrystalline structure varied randomly in the model in the range of $\pm 10\%$ of the average values presented in Table 1.

The spread of elastic and plastic properties from minimum to maximum values was about 20%.

2.4. Generation of Polycrystalline Structure and Mesh Convergence of the Solution

A three-dimensional polycrystalline structure containing 125 grains was built using the step-by-step packing method, which includes the following steps.

1. The computational domain is discretized by a rectangular mesh with step h . The mesh node coordinates in the Cartesian system are determined by the relationships

$$x^{[ijk]} = (i-1)h, y^{[ijk]} = (j-1)h, z^{[ijk]} = (k-1)h, \quad (11)$$

where $i = 1, \dots, N_x, j = 1, \dots, N_y, k = 1, \dots, N_z$ are the node indices along the X, Y , and Z coordinate axes, and N_x, N_y, N_z are the number of nodes in the respective directions. The cell center coordinates are defined as

$$\begin{aligned} X^{[ijk]} &= (i-1)h + \frac{h}{2}, \\ Y^{[ijk]} &= (j-1)h + \frac{h}{2}, \\ Z^{[ijk]} &= (k-1)h + \frac{h}{2}, \end{aligned} \quad (12)$$

where $i = 1, \dots, N_x-1, j = 1, \dots, N_y-1, k = 1, \dots, N_z-1$.

2. Grains grow by the spherical law. At each step of the procedure, the radii of the circles r_l around the grain nucleation sites increase by Δr :

$$r_l^n = r_l^{n-1} + \Delta r, l = 1, \dots, N_c, \quad (13)$$

where $\Delta r < h/\sqrt{2}$, and N_c is the number of nucleation sites.

3. For all cells not belonging to any of the grains, it is checked whether the coordinates of their centers fall into any of the domains

$$(X^{[ijk]} - X_l)^2 + (Y^{[ijk]} - Y_l)^2 + (Z^{[ijk]} - Z_l)^2 \leq r_l^2, \quad (14)$$

where X_l, Y_l, Z_l are the coordinates of the nucleus l . If condition (14) is satisfied, the cell is attached to the corresponding growing grain and excluded from the verification. The termination criterion for the generation procedure is the absence of cells that do not belong to any of the grains. The growth of equiaxed grains at the same rate corresponds to the crystallization conditions with uniform cooling without high

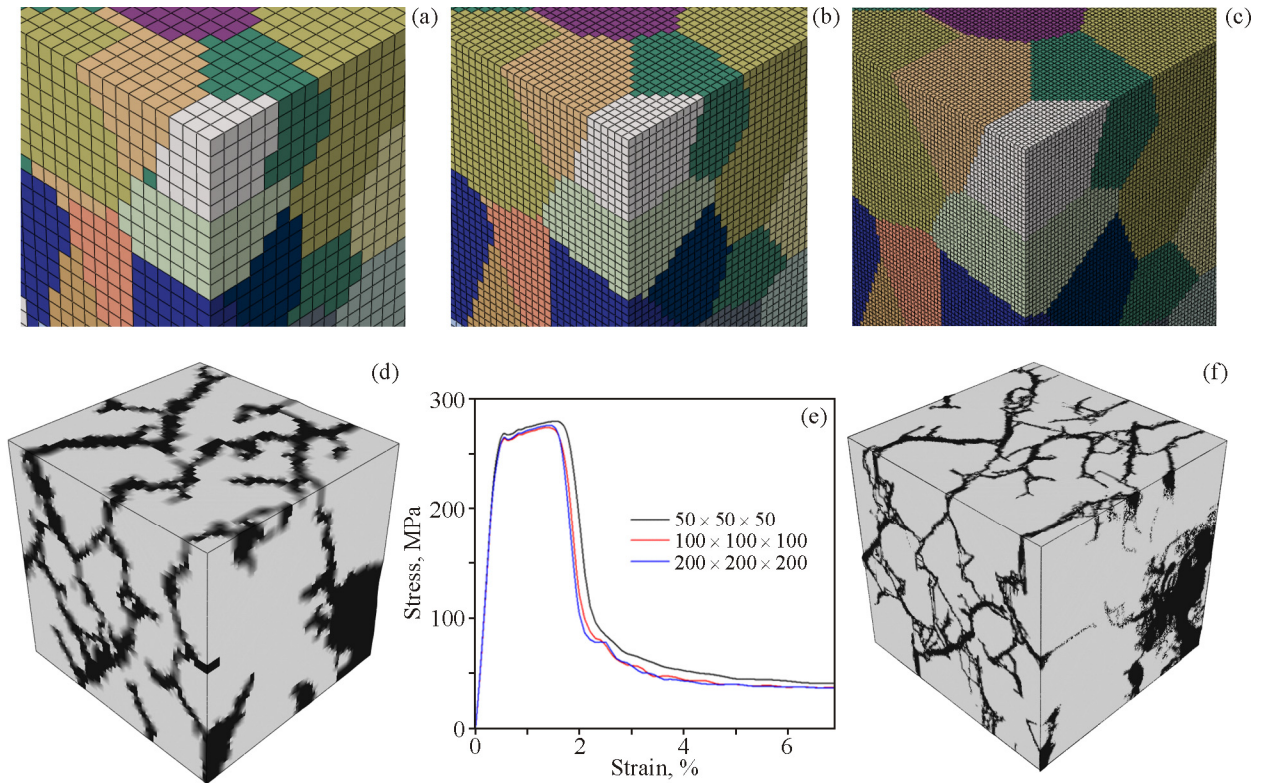


Fig. 3. Polycrystalline structures approximated by meshes with dimensions of $50 \times 50 \times 50$ (a), $100 \times 100 \times 100$ (b), and $200 \times 200 \times 200$ (c), crack distribution for meshes of $50 \times 50 \times 50$ (d) and $200 \times 200 \times 200$ (f), corresponding averaged tensile flow curves (e). Strain rate 3000 s^{-1} (color online).

temperature gradients, when all growing grains are under the same thermal conditions.

For checking the mesh convergence, the nucleation site coordinates (12) were retained. The mesh size was changed, and the law of grain growth re-

mained the same. The mesh convergence was studied under uniaxial tension using three models with the same microstructure, approximated by cubic cells with dimensions $50 \times 50 \times 50$, $100 \times 100 \times 100$, and $200 \times 200 \times 200$ (Figs. 3a–3c). The corresponding

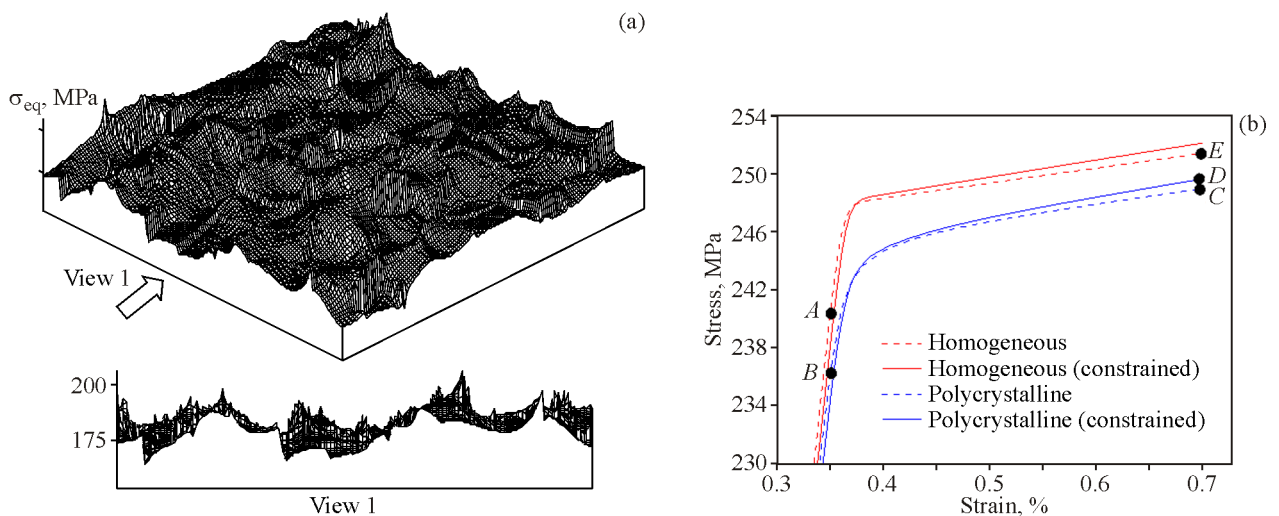


Fig. 4. Stress distribution at the elastic stage of polycrystal deformation (a) and averaged tensile flow curves for a homogeneous and polycrystalline samples with free boundaries and boundaries constrained in one of the directions (b). Strain rate 10 s^{-1} (color online).

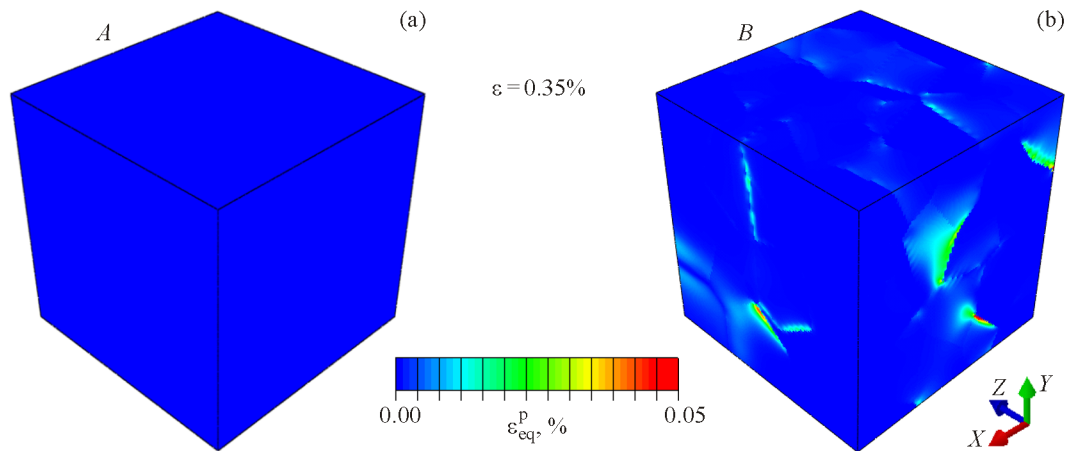


Fig. 5. Plastic strain distribution in a homogeneous sample (a) and a sample with a polycrystalline structure (b). Strain rate 10 s^{-1} (color online).

crack distributions, which are qualitatively close, are shown in Figs. 3d and 3f. The convergence of the flow curves with mesh refinement is presented in Fig. 3e. Thus, it was established that a $100 \times 100 \times 100$ mesh is optimal for calculations in terms of the balance between time costs and the level of detail of the simulation results. Calculations with a $200 \times 200 \times 200$ mesh require an order of magnitude longer computation time and larger data storage space, and significantly slow down data visualization and processing.

3. SIMULATION RESULTS

3.1. Plastic Strain Localization

Deformation behavior was analyzed comparatively between a homogeneous sample (HS) and a polycrystalline sample (PS). The samples were subjected to dynamic tension to the same macroscopic strain. The elastic and plastic properties of the PS were randomly varied in the grains of the polycrystalline microstructure within the 10% range relative to the average values for the HS given in Table 1. Analysis of the simulation results showed the following. At the elastic stage of deformation, the stress-strain state of the PS is inhomogeneous due to the difference in the elastic moduli of the grains (Fig. 4a, the state at 0.26% strain on the blue curve in Fig. 4b). While the HS is still undergoing elastic deformation, the PS exhibits local regions of incipient plastic deformation (Fig. 5). These regions appear already at the stage of deformation when the average stress level is below the lowest yield strength for grains, which is due to the appearance of stress concentrators at grain

boundaries and triple junctions. This causes a deviation from the linear elastic behavior on the macroscopic flow curve of the PS (Fig. 4b), while the HS continues to deform purely elastically.

With further increase in load, the grains are sequentially involved in the plastic flow, depending on the value of the yield strength. Plastic deformation in grains with lower yield strength continues to propagate into the grain bulk, and new localization sites appear in grains with higher yield strength at triple junctions. It is noteworthy that in the case of fully developed plastic flow, when the entire HS experiences large plastic strains, there are still local regions of elastic deformation in the PS (Fig. 6c), which persist in grains with the highest yield strength up to 1% of the total strain of the sample. The maximum local values of the equivalent plastic strains at this stage of loading can exceed the average value by a factor of 2–3 (Figs. 6b and 6c).

It was found that the imposed quasi-plane strain conditions in the constrained sample lead to the formation of elongated localization zones where plastic strains are close in value, while in the unconstrained sample the size of plastic strain localization zones is comparable in all three directions (Figs. 6c and 6d). The plastic strain localization zones in the planes subjected to constrained boundary conditions extend at an angle of 45° to the loading axis. It is shown that the degree of plastic strain localization in bands in the constrained sample is higher than in unconstrained samples. As a result, the material under constrained conditions is more strengthened and shows a higher stress level on the macroscopic flow curve (Fig. 4b).

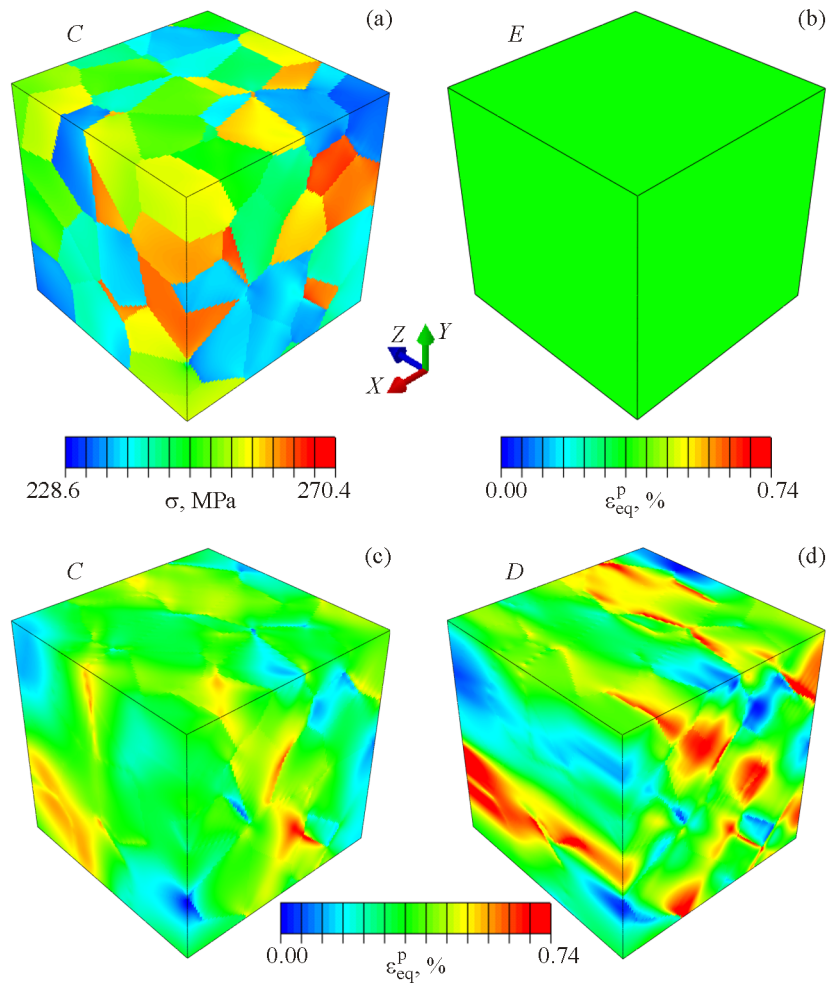


Fig. 6. Equivalent stress distribution in the sample with a polycrystalline structure (a) and plastic strain distribution in the homogeneous sample (b). Equivalent plastic strain distribution in the polycrystalline sample without additional boundary conditions (c) and under constrained conditions (d). Strain rate 10 s^{-1} (color online).

3.2. Effect of the Loading Rate on the Fracture of Polycrystalline Aluminum

The fracture process was investigated on the same polycrystalline sample using the same relaxation model (1), (5), but taking into account the local strain fracture criterion (6).

The study of the relationship between the volume fraction of fractured material and the degree and rate of deformation in the range from 10 to 5000 s^{-1} revealed that the volume fraction of fractured material in the sample increases with increasing strain rate (Fig. 7).

At a strain rate of 10 s^{-1} , a crack initiates in the sample and propagates in a plane perpendicular to the loading direction, dividing the sample into two parts (Fig. 8a). Above strain rates of the order of 100 s^{-1} , additional local fracture sites appear, giving rise to multiple cracking (Figs. 8b and 8c). This is due to the

fact that at low loading rates release waves from the primary crack have time to unload other regions of local stress concentration before the equivalent plastic strain in them exceeds the critical value. The cross-sectional configurations (Figs. 8a–8c) are chosen so as to show the crack propagation in the sample. At a low strain rate (10 s^{-1}), the crack grows through the entire sample, through the plane perpendicular to the tensile axis. Secondary crack initiation sites appear as the strain rate increases. As a result, the distribution of cracks is uneven.

The higher the strain rate, the higher the rate of increase in local stresses in the concentration regions and, accordingly, the rate of plastic strain accumulation. The unloading waves from the local regions, which are the first to fracture, do not have time to unload other stress concentration regions before the critical strains are accumulated in them. Thus, the accu-

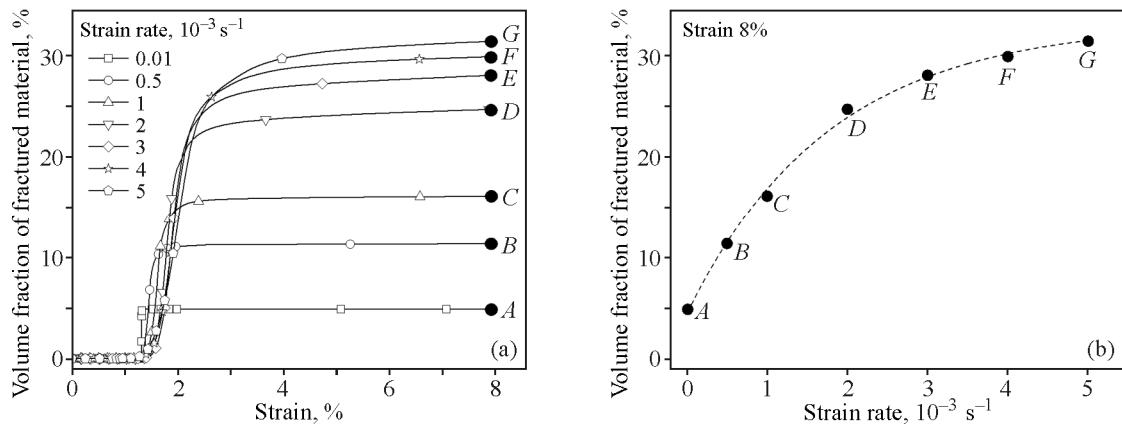


Fig. 7. Dependence of the volume fraction of fractured material on strain (a) and strain rate (b).

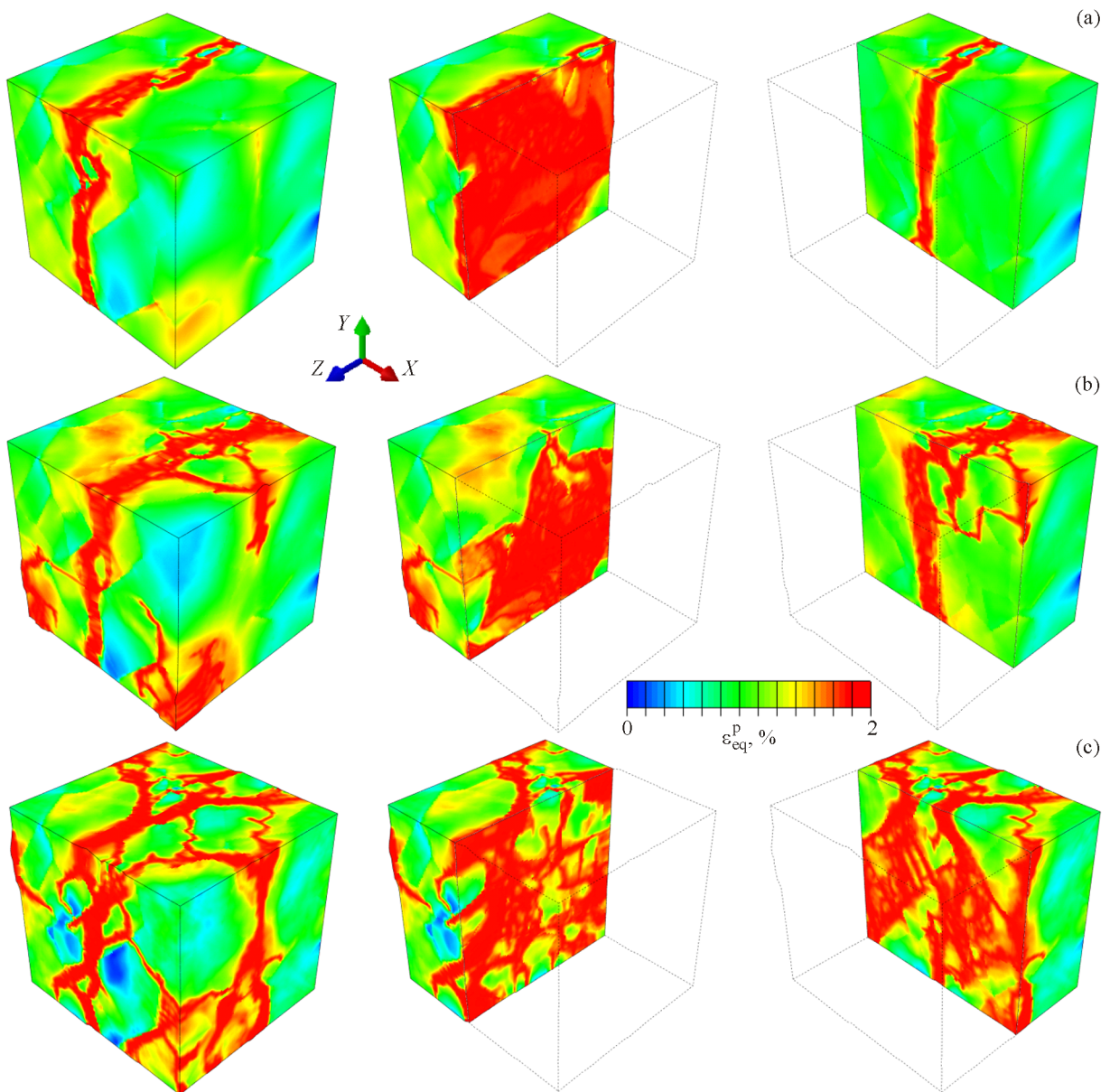


Fig. 8. Distribution of cracks in a tensile polycrystalline sample stretched to 8% strain at rates 10 (a), 500 (b), 5000 s^{-1} (c) (color online).

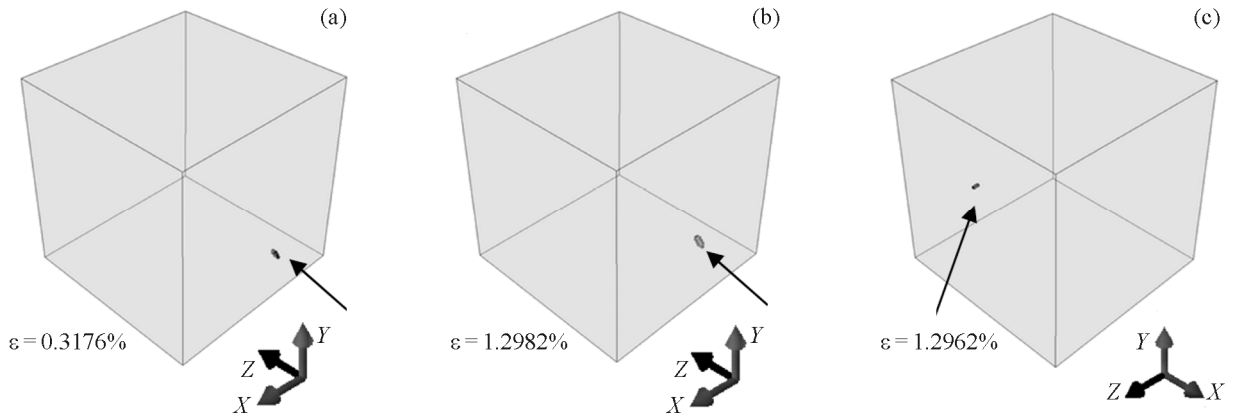


Fig. 9. Crack initiation in model samples at strain rates of 10 (a), 2000 (b), and 3000 s⁻¹ (c).

ulated equivalent plastic strain exceeds the critical value successively in several regions. The higher the strain rate, the greater the number of crack initiation sites. The sample breaks into several pieces as a result of multiple cracking (Figs. 8b and 8c). The numerical simulation showed that the effect of the stra-

in rate in the range from 10 to 2000 s⁻¹ on the pattern and degree of plastic strain localization in the sample at the prefracture stage is insignificant, and therefore the primary crack initiates at the same boundary between grains (Figs. 9a and 9b). At strain rates above 3000 s⁻¹, the influence of wave dynamics becomes

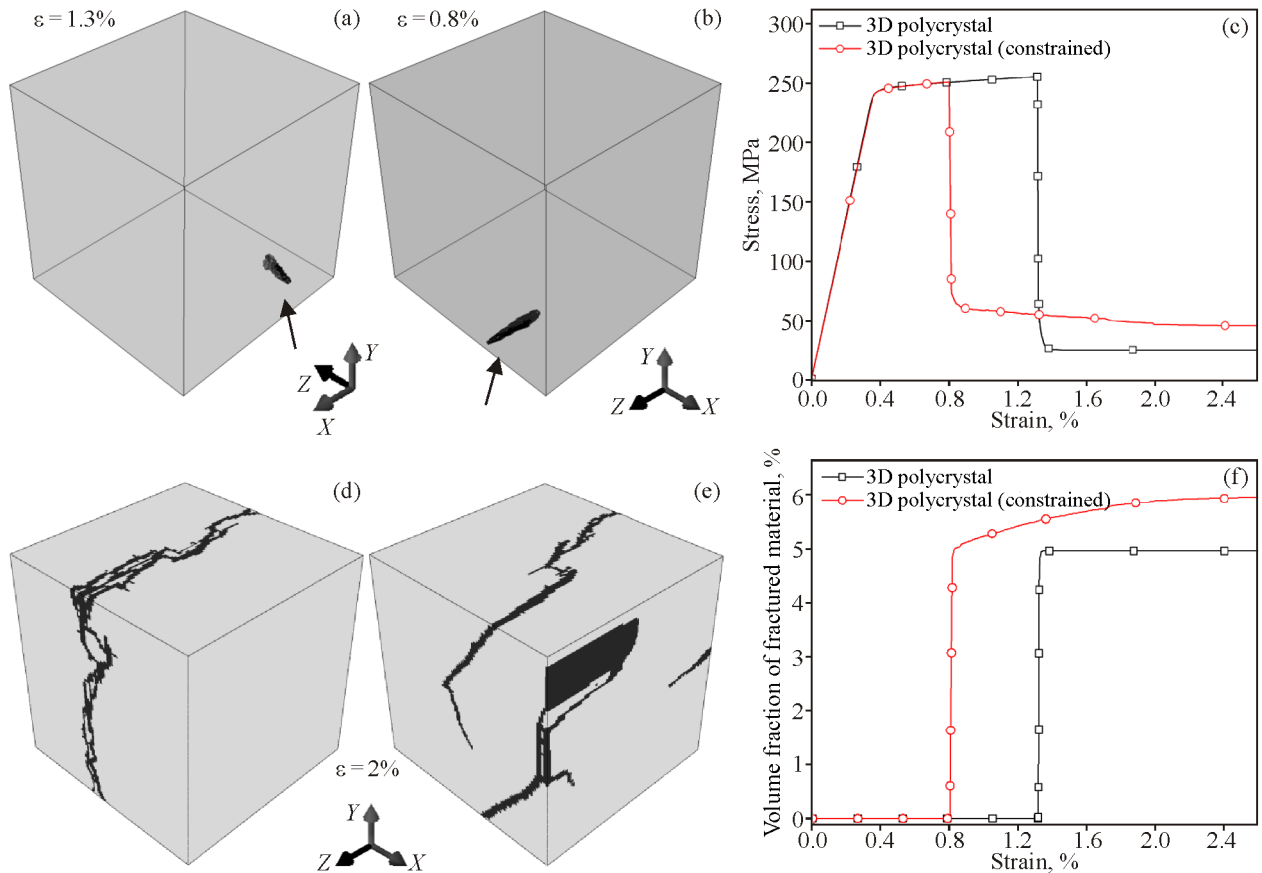


Fig. 10. Crack initiation and growth in samples with free boundaries (a, d) and under constrained deformation conditions (b, e). The strain dependence of the average stress (c) and volume fraction of fractured material (f). Strain rate 10 s⁻¹ (color online).

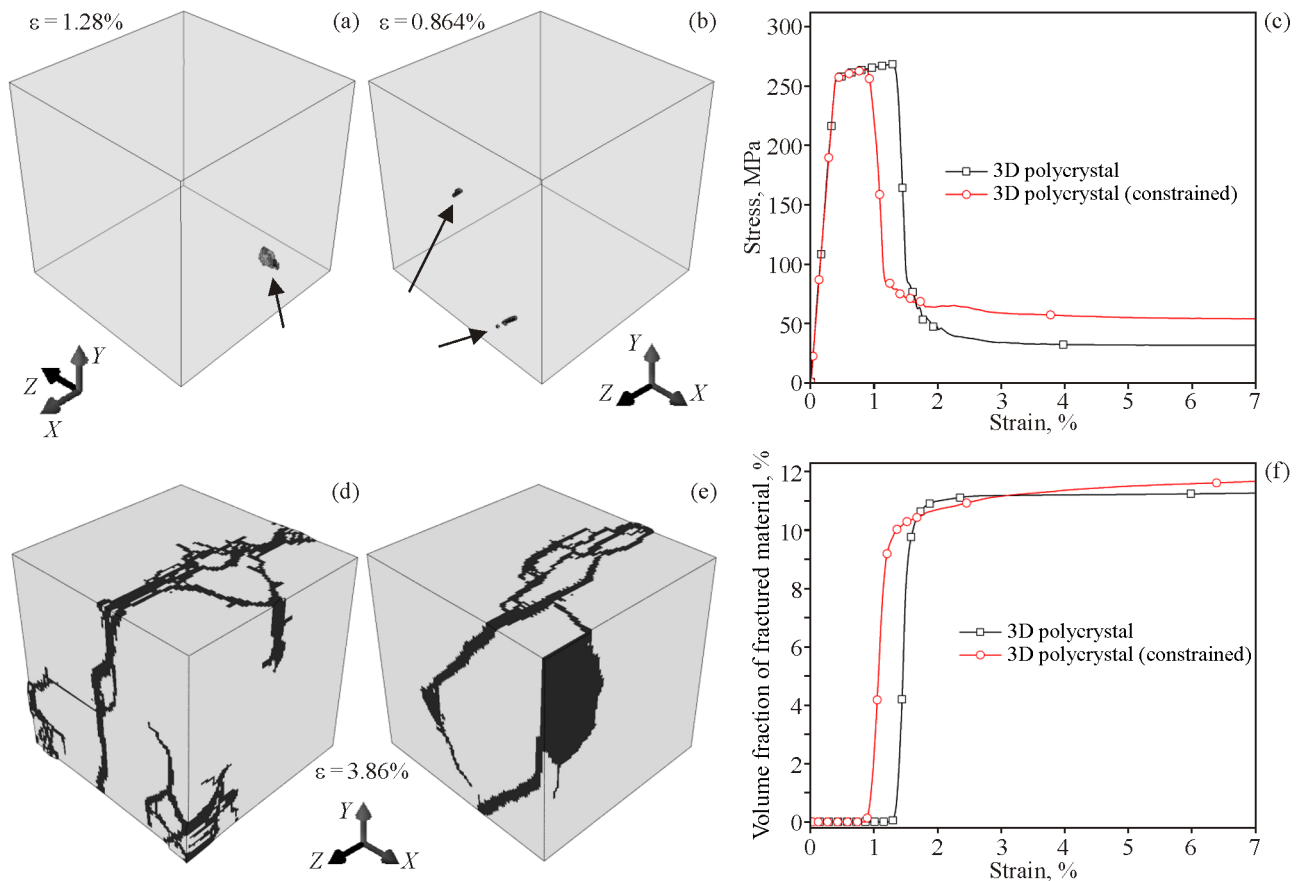


Fig. 11. Crack initiation and growth in samples with free boundaries (a, d) and under constrained deformation conditions (b, e). The strain dependence of the average stress (c) and volume fraction of fractured material (f). Strain rate 500 s^{-1} (color online).

more prominent than the influence of structural heterogeneity, and that is why the primary crack initiates at a different site (Fig. 9c).

3.3. Effect of Deformation Constraint on the Fracture of Polycrystalline Aluminum

Constrained boundary conditions simulating quasi-plane strain are an additional factor affecting the stress concentration, plastic strain localization, and fracture behavior. Due to the higher equivalent plastic strains in the strain localization zones, a crack in the constrained sample initiates earlier than in the sample with free side surfaces (Figs. 10–12). The crack initiation sites are different in these two samples (Figs. 10–12). The cracks propagate along plastic strain localization bands formed before fracture (Figs. 10–12).

At a strain rate of 10 s^{-1} , two cracks are formed in the simulations with constrained boundary conditions. One of them reaches the loaded surface. The cracks propagate at an angle of 45° to the loading

axis in planes perpendicular to the Z axis (Fig. 10e). These results are different from the results obtained for the sample with free side surfaces, where one crack propagates in a plane perpendicular to the tensile axis (Fig. 10d).

At a strain rate of 500 s^{-1} , multiple cracking occurs even in the unconstrained sample. The constrained sample shows qualitatively the same fracture pattern as in the case with a strain rate of 10 s^{-1} . One of the cracks propagates to the loaded surface. In planes perpendicular to the Z axis, cracks propagate at an angle of 45° to the loading axis (Fig. 11e). This pattern is also different from the case with free side surfaces where multiple cracks propagate perpendicular to the loading direction.

At a strain rate of 3000 s^{-1} , cracking is more pronounced in the zones of plastic strain localization, which are formed under constrained deformation. Cracks propagate at an angle of 45° to the loading axis in planes parallel to the constrained side surfaces (Fig. 12e). In planes parallel to free surfaces, cracks propagate perpendicular to the tensile direction from

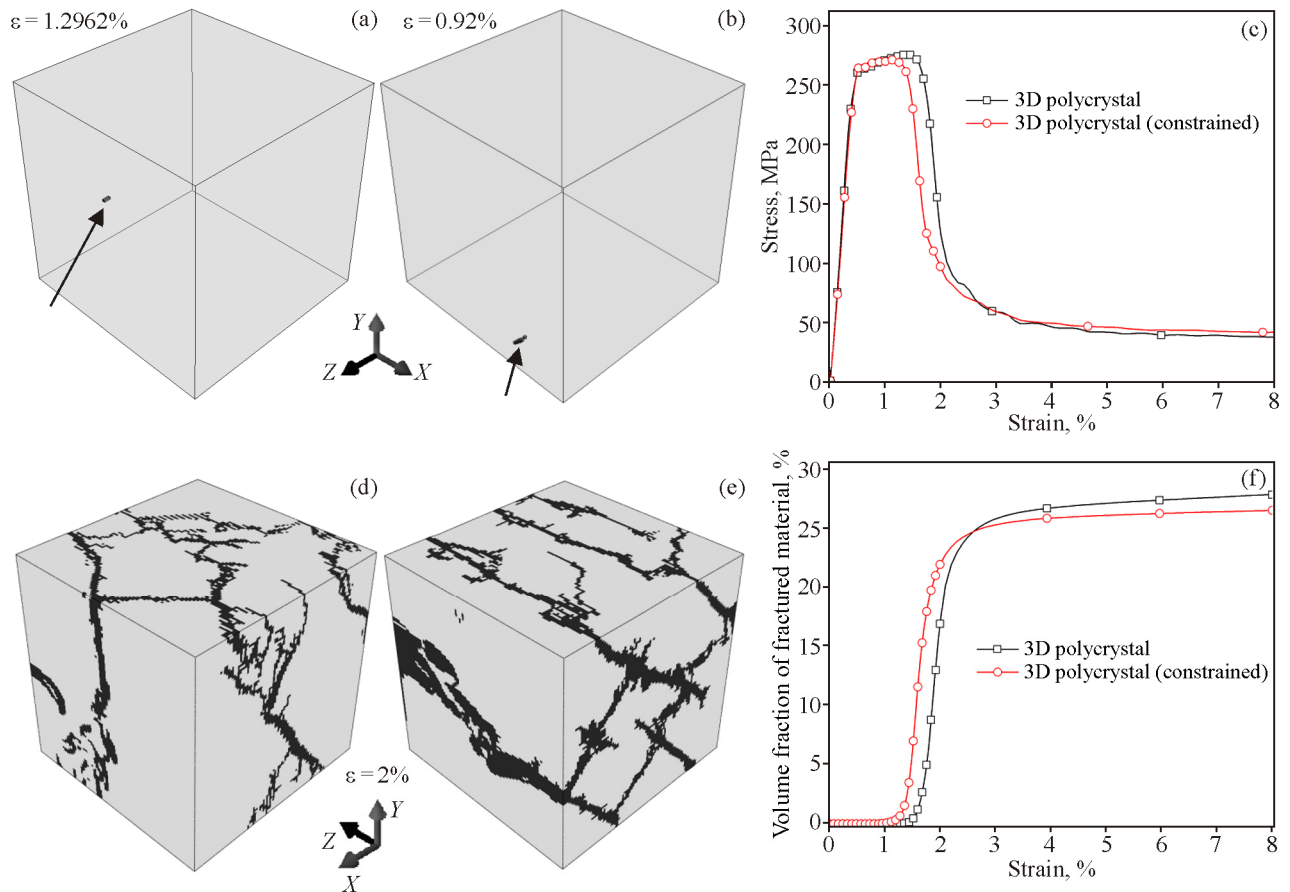


Fig. 12. Crack initiation and growth in samples with free boundaries (a, d) and under constrained deformation conditions (b, e). The strain dependence of the average stress (c) and volume fraction of fractured material (f). Strain rate 3000 s^{-1} (color online).

one constrained surface to the opposite. Thus, in the case of constrained boundary conditions, three-dimensional cracks are flat cracks conjugated in perpendicular directions and oriented at an angle of 45° to the loading axis. The primary crack initiates earlier in the constrained sample both at a strain rate of 10 s^{-1} and at 500 and 3000 s^{-1} . This is because the constrained surfaces do not generate unloading waves (Figs. 10a, 10b, 11a, 11b, 12a, 12b).

The volume fraction of fractured material in the constrained sample at a strain rate of 10 s^{-1} is larger than in the sample with free side surfaces during the entire loading process (Fig. 10f). A different fracture scenario is observed at a strain of 500 s^{-1} , where the curves of fractured material volume versus strain intersect twice: the volume of fractured material under constrained conditions is larger everywhere, except for the strain range between the intersection points (Fig. 11f). At a strain rate of 3000 s^{-1} , the curves intersect once; the fractured material volume in the constrained sample is larger up to the point of intersection and lower after the point, corresponding to

approximately 2.6% strain (Fig. 12f). Finally, we can conclude that constrained deformation conditions have a negative effect at low strain rates, leading to more rapid fracture of the polycrystal. At medium strain rates, there is a strain range in which the crack growth rate in constrained regions of the loaded material can be reduced. At high loading rates, constrained conditions have a negative effect at the initial stages of fracture, but can inhibit cracking in the regions of intense deformation of a polycrystalline material.

4. CONCLUSIONS

A relaxation constitutive equation for multidimensional flows was derived on the basis of a physically justified model. The thermomechanical model parameters for 6061-T6 aluminum alloy were determined in the range of strain rates of 0.01 – 500 s^{-1} and temperatures of 77 – 430 K . The mesh convergence of the solution for the fracture of samples was studied with explicit allowance for the polycrystalline structure,

and the optimal size of the computational mesh was determined.

Numerical analysis was performed to investigate the effect of microstructure, strain rate, and constrained boundary conditions, which simulate quasi-plane strain, on the deformation and fracture of polycrystalline aluminum. It was found that taking into account the polycrystalline structure leads to the formation of plastic strain localization sites in the early stages of loading, when a homogeneous sample is still at the stage of elastic deformation. In the case of fully developed plastic flow, when the entire homogeneous sample already experiences large plastic strains, the polycrystal still exhibits local regions of elastic deformation. Taking into account the polycrystalline structure of the samples leads to lower values of the macroscopic flow stress.

At a strain rate of 10 s^{-1} , a crack initiates and propagates in a plane perpendicular to the loading axis. As the strain rate increases to a threshold value of 100 s^{-1} , additional local fracture sites appear and multiple cracking occurs in the sample. At strain rates above 2000 s^{-1} , the influence of wave dynamics becomes more significant than the influence of structural heterogeneity, and therefore the primary crack initiates at a different site in the sample.

It is shown that constrained boundary conditions strongly affect the plastic strain localization and fracture behavior of polycrystalline aluminum. Three-dimensional cracks under such conditions are conjugated flat cracks propagating at an angle of 45° to the loading axis. Constrained conditions accelerate the fracture of the material at low strain rates in the entire strain range, and can inhibit the growth of main cracks at medium and high strain rates.

FUNDING

The work was carried out under the government statement of work for ISPMS SB RAS, research line No. FWRW-2021-0002.

REFERENCES

1. *Aluminum and Aluminum Alloys: ASM Specialty Handbook*, Davis, J.R., Ed., Chagrin Falls, Ohio: ASM Int., 1993.
2. Benedyk, J.C., Aluminum Alloys for Lightweight Automotive Structures, in *Design and Manufacturing for Lightweight Vehicles*, USA: Woodhead Publishing, 2010, pp. 79–113. <https://doi.org/10.1533/9781845697822.1.79>
3. Estrin, Y., Murashkin, M., and Valiev, R., Ultrafine-Grained Aluminium Alloys: Processes, Structural Features and Properties, in *Fundamentals of Aluminum Metallurgy*, UK: Woodhead Publishing, 2010, pp. 468–497. <https://doi.org/10.1533/9780857090256.2.468>
4. Trusov, P.V., Ostanina, T.V., and Shveykin, A.I., Evolution of the Grain Structure of Metals and Alloys under Severe Plastic Deformation: Continuum Models, *PNRPU Mech. Bull.*, 2022, no. 1, pp. 123–155. <https://doi.org/10.15593/perm.mech/2022.1.11>
5. Shin, H. and Kim, J.B., A Phenomenological Constitutive Equation to Describe Various Flow Stress Behaviors of Materials in Wide Strain Rate and Temperature Regimes, *J. Eng. Mater. Technol.*, 2010, vol. 132, no. 2, p. 021009. <https://doi.org/10.1115/1.4000225>
6. Lin, Y.C. and Chen, X.-M., A Critical Review of Experimental Results and Constitutive Descriptions for Metals and Alloys in Hot Working, *Mater. Design*, 2011, vol. 32, no. 4, pp. 1733–1759. <https://doi.org/10.1016/j.matdes.2010.11.048>
7. Johnson, G.R. and Cook, W.H., A Constitutive Model and Data for Metals Subjected to Large Strains, High Strain Rates and High Temperatures, in *Proc. 7th Int. Symp. Ballistics*, Arlington, VA: American Defense Preparedness Association, 1983, pp. 541–547.
8. Khan, A.S. and Huang, S., Experimental and Theoretical Study of Mechanical Behavior of 1100 Aluminum in the Strain Rate Range 10^{-5} – 10^{-4} s^{-1} , *Int. J. Plasticity*, 1992, vol. 8, pp. 397–424. [https://doi.org/10.1016/0749-6419\(92\)90057-J](https://doi.org/10.1016/0749-6419(92)90057-J)
9. Khan, A.S., Zhang, H.Y., and Takacs, L., Mechanical Response and Modeling of Fully Compacted Nanocrystalline Iron and Copper, *Int. J. Plasticity*, 2000, vol. 16, pp. 1459–1476. [https://doi.org/10.1016/S0749-6419\(00\)00023-1](https://doi.org/10.1016/S0749-6419(00)00023-1)
10. Bodner, S.R. and Partom, Y., Constitutive Equation for Elastoviscoplastic Strain Hardening Material, *J. Appl. Mech.*, 1975, pp. 385–389. <https://doi.org/10.1115/1.3423586>
11. Fields, D.S. and Bachofen, W.A., Determination of Strain Hardening Characteristics by Torsion Testing, *Proc. Am. Soc. Test. Mater.*, 1957, vol. 57, pp. 1259–1272.
12. Rudnytskyj, A., Simon, P., Jech, M., and Gachot, C., Constitutive Modelling of the 6061 Aluminium Alloy under Hot Rolling Conditions and Large Strain Ranges, *Mater. Design*, 2020, vol. 190, p. 108568. <https://doi.org/10.1016/j.matdes.2020.108568>
13. Pandya, K.S., Roth, Ch.C., and Mohr, D., Strain Rate and Temperature Dependent Fracture of Aluminum Alloy 7075: Experiments and Neural Network Modeling, *Int. J. Plasticity*, 2020, vol. 135, p. 102788. <https://doi.org/10.1016/j.ijplas.2020.102788>
14. Zerilli, P.J. and Armstrong, R.W., Dislocation-Mechanics-Based Constitutive Relations for Material Dynamics Calculations, *J. Appl. Phys.*, 1987, vol. 61, pp. 1816–1825. <https://doi.org/10.1063/1.338024>

15. Lin, Y.C., Chen, M.S., and Zhang, J., Prediction of 42CrMo Steel Flow Stress at High Temperature and Strain Rate, *Mech. Res. Commun.*, 2008, vol. 35, pp. 142–150. <https://doi.org/10.1016/j.mechrescom.2007.10.002>
16. Preston, D.L., Tonks, D.L., and Wallace, D.C., Model of Plastic Deformation for Extreme Loading Conditions, *J. Appl. Phys.*, 2003, vol. 93, pp. 211–220. <https://doi.org/10.1063/1.1524706>
17. Rusinek, A. and Klepaczko, J.R., Shear Testing of a Sheet Steel at Wide Range of Strain Rates and a Constitutive Relation with Strain-Rate and Temperature Dependence of the Flow Stress, *Int. J. Plasticity*, 2001, vol. 17, pp. 87–115. [https://doi.org/10.1016/S0749-6419\(00\)00020-6](https://doi.org/10.1016/S0749-6419(00)00020-6)
18. Voyiadjis, G.Z. and Almasri, A.H., A Physically Based Constitutive Model for FCC Metals with Applications to Dynamic Hardness, *Mech. Mater.*, 2008, vol. 40, pp. 549–563. <https://doi.org/10.1016/j.mechmat.2007.11.008>
19. Nemat-Nasser, S. and Guo, W.G., Thermomechanical Response of HSLA-65 Steel Plates: Experiment and Modeling, *Mech. Mater.*, 2005, vol. 37, pp. 379–405. <https://doi.org/10.1016/j.mechmat.2003.08.017>
20. Balokhonov, R.R., Romanova, V.A., and Schmauder, S., Finite-Element and Finite-Difference Simulations of the Mechanical Behavior of Austenitic Steels at Different Strain Rates and Temperatures, *Mech. Mater.*, 2009, vol. 41, no. 1, pp. 1277–1287. <https://doi.org/10.1016/j.mechmat.2009.08.005>
21. Kim, J. and Yoon, J.W., Necking Behavior of AA 6022-T4 Based on the Crystal Plasticity and Damage Models, *Int. J. Plasticity*, 2015, vol. 73, pp. 3–23. <https://doi.org/10.1016/j.ijplas.2015.06.013>
22. Proudhon, H., Li, J., Wang, F., Roos, A., Chiaruttini, V., and Forest, S., 3D Simulation of Short Fatigue Crack Propagation by Finite Element Crystal Plasticity and Remeshing, *Int. J. Fatigue*, 2016, vol. 82, pp. 238–246. <https://doi.org/10.1016/j.ijfatigue.2015.05.022>
23. Dai, Q., Deng, Y., Jiang, H., Tang, J., and Chen, J., Hot Tensile Deformation Behaviors and a Phenomenological AA5083 Aluminum Alloy Fracture Damage Model, *Mater. Sci. Eng. A*, 2019, vol. 766, p. 138325. <https://doi.org/10.1016/j.msea.2019.138325>
24. Tasan, C.C., Hoefnagels, J.P.M., Diehl, M., Yan, D., Roters, F., and Raabe, D., Strain Localization and Damage in Dual Phase Steels Investigated by Coupled In-Situ Deformation Experiments and Crystal Plasticity Simulations, *Int. J. Plasticity*, 2014, vol. 63, pp. 198–210. <https://doi.org/10.1016/j.ijplas.2014.06.004>
25. Mason, J.K., Lind, J., Li, S.F., Reed, B.W., and Kumar, M., Kinetics and Anisotropy of the Monte Carlo Model of Grain Growth, *Acta Mater.*, 2015, vol. 82, pp. 155–166. <https://doi.org/10.1016/j.actamat.2014.08.063>
26. Jacot, A. and Rappaz, M., A Pseudo-Front Tracking Technique for the Modelling of Solidification Microstructures in Multi-Component Alloys, *Acta Mater.*, 2002, vol. 50, pp. 1902–1926. [https://doi.org/10.1016/S1359-6454\(01\)00442-6](https://doi.org/10.1016/S1359-6454(01)00442-6)
27. Guilhem, Y., Basseville, S., Curtit, F., Stéphan, J.-M., and Cailletaud, G., Numerical Investigations of the Free Surface Effect in Three-Dimensional Polycrystalline Aggregates, *Comp. Mater. Sci.*, 2013, vol. 70, pp. 150–162. <https://doi.org/10.1016/j.commatsci.2012.11.052>
28. Zhang, T., Lu, Sh., Wu, Yu., and Gong, H., Optimization of Deformation Parameters of Dynamic Recrystallization for 7055 Aluminum Alloy by Cellular Automaton, *Trans. Nonferr. Met. Soc. China*, vol. 27, no. 6, pp. 1327–1337. [https://doi.org/10.1016/S1003-6326\(17\)60154-7](https://doi.org/10.1016/S1003-6326(17)60154-7)
29. Romanova, V.A., Balokhonov, R.R., and Schmauder, S., Numerical Study of Mesoscale Surface Roughening in Aluminum Polycrystals under Tension, *Mater. Sci. Eng. A*, 2013, vol. 564, pp. 255–263. <https://doi.org/10.1016/j.msea.2012.12.004>
30. Lim, H., Battaile, C.C., Bishop, J.E., and Foulk III, J.W., Investigating Mesh Sensitivity and Polycrystalline RVEs in Crystal Plasticity Finite Element Simulations, *Int. J. Plasticity*, 2019, vol. 121, pp. 101–115. <https://doi.org/10.1016/j.ijplas.2019.06.001>
31. Liu, X., Sun, W.K., and Liew, K.M., Multiscale Modeling of Crystal Plastic Deformation of Polycrystalline Titanium at High Temperatures, *Comp. Meth. Appl. Mech. Eng.*, 2018, vol. 340, pp. 932–955. <https://doi.org/10.1016/j.cma.2018.06.026>
32. Tian, Y., Ding, J., Huang, X., Zheng, H.-R., Song, K., Lu, S., and Zeng, X., Plastic Deformation Mechanisms of Tension-Compression Asymmetry of Nanopolycrystalline TiAl: Twin Boundary Spacing and Temperature Effect, *Comput. Mater. Sci.*, 2020, vol. 171, p. 109218. <https://doi.org/10.1016/j.commatsci.2019.109218>
33. Cyr, E., Mohammadi, M., Mishra, R.K., and Inal, K., A Three Dimensional (3D) Thermo-Elasto-Viscoplastic Constitutive Model for FCC Polycrystals, *Int. J. Plasticity*, 2015, vol. 70, pp. 166–190. <https://doi.org/10.1016/j.ijplas.2015.04.001>
34. Gao, T.J., Zhao, D., Zhang, T.W., Jin, T., Ma, S.G., and Wang, Z.H., Strain-Rate-Sensitive Mechanical Response, Twinning, and Texture Features of NiCo-CrFe High-Entropy Alloy: Experiments, Multi-Level Crystal Plasticity and Artificial Neural Networks Modeling, *J. Alloys Compnd.*, 2020, vol. 845, p. 155911. <https://doi.org/10.1016/j.jallcom.2020.155911>
35. Wang, Y., Lei, J., Bai, L., Zhou, K., and Liu, Z., Effects of Tensile Strain Rate and Grain Size on the Mechanical Properties of Nanocrystalline T-Carbon, *Comput. Mater. Sci.*, 2019, vol. 170, p. 109188. <https://doi.org/10.1016/j.commatsci.2019.109188>
36. Zhang, T., Zhou, K., and Chen, Z., Strain Rate Effect on Plastic Deformation of Nanocrystalline Copper Investigated by Molecular Dynamics, *Mater. Sci. Eng.*,

- 2015, vol. 648, pp. 23–30. <https://doi.org/10.1016/j.msea.2015.09.035>
37. Lim, H., Jong Bong, H., Chen, S.R., Rodgers, T.M., Battaile, C.C., and Lane, J.M.D., Developing Anisotropic Yield Models of Polycrystalline Tantalum Using Crystal Plasticity Finite Element Simulations, *Mater. Sci. Eng.*, 2018, vol. 730, pp. 50–56. <https://doi.org/10.1016/j.msea.2018.05.096>
38. Hu, P., Liu, Y., Zhu, Y., and Ying, L., Crystal Plasticity Extended Models Based on Thermal Mechanism and Damage Functions: Application to Multiscale Modeling of Aluminum Alloy Tensile Behavior, *Int. J. Plasticity*, 2016, vol. 86, pp. 1–25. <https://doi.org/10.1016/j.ijplas.2016.07.001>
39. Romanova, V.A., Balokhonov, R.R., Shakhidzhinov, V.S., Vlasov, I.V., Moskvichev, E.N., and Nekhorosheva, O., Evolution of Mesoscopic Deformation-Induced Surface Roughness and Local Strains in Tensile Polycrystalline Aluminum, *Phys. Mesomech.*, 2021, vol. 24, no. 5, pp. 570–577. <https://doi.org/10.1134/S1029959921050088>
40. Balokhonov, R., Romanova, V., Zinovieva, O., and Dymnich, E., A Computational Study of the Effects of Polycrystalline Structure on Residual Stress-Strain Concentrations and Fracture in Metal-Matrix Composites, *Eng. Failure Analys.*, 2022, vol. 138, p. 106379. <https://doi.org/10.1016/j.engfailanal.2022.106379>
41. Balokhonov, R., Romanova, V., Zinovieva, O., and Zemlianov, A., Microstructure-Based Analysis of Residual Stress Concentration and Plastic Strain Localization Followed by Fracture in Metal-Matrix Composites, *Eng. Fract. Mech.*, 2021, p. 108138. <https://doi.org/10.1016/j.engfracmech.2021.108138>
42. Romanova, V., Balokhonov, R., Zinovieva, O., Emelianova, E., Dymnich, E., Pisarev, M., and Zinoviev, A., Micromechanical Simulations of Additively Manufactured Aluminum Alloys, *Comp. Struct.*, 2021, vol. 244, p. 106412. <https://doi.org/10.1016/j.compstruc.2020.106412>